Fast Ion Conduction and Its Origin in $Li_{6-x}PS_{5-x}Br_{1+x}$

Pengbo Wang, Haoyu Liu, Sawankumar Patel, Xuyong Feng, Po-Hsiu Chien, Yan Wang, and Yan-Yan Hu*
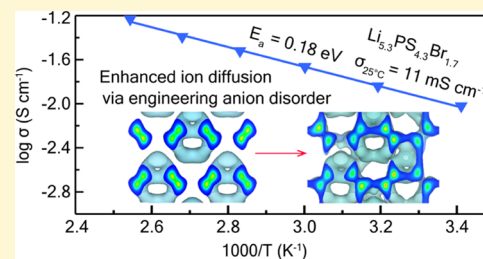
Read Online

ACCESS | Metrics & More | Article Recommendations | Supporting Information

ABSTRACT: High ionic conductivity of solid electrolytes is key to achieving high-power all-solid-state rechargeable batteries. The superionic argyrodite family is among the most conductive Li-ion conductors. However, their potential in ionic conductivity and stability is far from being reached, especially with Li_6PS_5Br. Here, we synthesized $Li_{6-x}PS_{5-x}Br_{1+x}$ with increased site mixing of Br^-/S^{2-}. An ionic conductivity of 11 mS cm^{-1} at 25 °C is achieved with a low activation energy of 0.18 eV for $Li_{5.3}PS_{4.3}Br_{1.7}$. The influence of Br^-/S^{2-} mixing on ion conduction is systematically investigated with multinuclear solid-state NMR coupled with X-ray diffraction and impedance spectroscopy. A statistically random distribution of Br^- and S^{2-} at 4d sites is observed with ^{31}P NMR. The resulting local structures regulate the jump rates of their neighboring Li ions and Li redistribution. As a result, the increased Li$^+$ occupancy at 24g sites promotes fast ion conduction, and the role of Li (24g) in ion conduction has been elucidated with tracer-exchange NMR. Experimental evidence combined with density functional theory calculations has revealed that the particular arrangement of 1S3Br at 4d sites near Li maximizes overall Li$^+$ conduction. This insight applies to other argyrodites and will be useful to the design of new fast ion conductors.

Graph in abstract: $E_a = 0.18$ eV, $Li_{5.3}PS_{4.3}Br_{1.7}$, $\sigma_{25°C} = 11$ mS cm^{-1}, "Enhanced ion diffusion via engineering anion disorder"; axes log σ (S cm^{-1}) vs 1000/T (K^{-1}).

INTRODUCTION

Solid electrolytes for rechargeable Li-ion batteries offer not only improved safety but also high energy density by enabling the potential use of high-voltage cathodes and metallic lithium anodes.[1−3]

High ionic conductivity is critical for high-power applications. Sulfide argyrodites (Li_6PS_5X, X = Cl, Br, and I) are among the most conductive Li$^+$ solid electrolytes.[4−12] Their ionic conductivity is largely dependent on S^{2-}/X^- mixing at 4d sites.[8,10,13−15] It has been reported that in Li_6PS_5I, 4d sites are exclusively occupied by S^{2-} (I (4d) = 0);[16] however, in Li_6PS_5Br and Li_6PS_5Cl, considerable site mixing of Br^-/Cl^- with S^{2-} (Cl (4d) = 63%, Br (4d) = 43%)[16] was found, which is positively correlated with the observed substantial increase in ionic conductivity of several orders of magnitude (4.6 × 10^{-7}, 7.2 × 10^{-4}, and 7.4 × 10^{-4} S/cm for Li_6PS_5I, Li_6PS_5Br, and Li_6PS_5Cl, respectively).[6,8,16] In addition, the distribution of Li in argyrodites is not trivial. Each unit cell of Li_6PS_5X holds 24 Li ions that partially occupy 24g and 48h sites, forming three different Li-ion hopping pathways: doublet, intracage, and intercage. All three jumps together form a network responsible for the long-range Li conduction.[15] The occupancy of 4d sites by halide ions can affect the distribution of Li over 24g and 48h sites, which in turn governs Li$^+$ transport.

In order to enhance ion conduction via increasing halide/S disorder, cation doping at P sites has been shown to be effective. A recent work on Ge-doped I-argyrodite with tuned I^-/S^{2-} mixing over 4a and 4d sites shows significantly enhanced ionic conductivity.[10] In this work, the anion-doping strategy is employed, and Br-rich $Li_{6-x}PS_{5-x}Br_{1+x}$ is synthesized to enforce anion and Li$^+$ disorder in the structural lattice. A maximum ionic conductivity of 11 mS cm^{-1} at 25 °C is achieved in $Li_{5.3}PS_{4.3}Br_{1.7}$. In order to further understand the origin of high ionic conductivity, we have utilized high-resolution solid-state NMR to unveil local structural disorder and defects.[17] Local atomic arrangements and statistically random distributions of distinctive configurations of 4d sites are elucidated. The correlations of ionic conductivity with Li and Br/S site disorder are investigated. The active Li structural positions to constitute ion transport pathways are identified with $^6Li \rightarrow {}^7Li$ tracer-exchange NMR. In conjunction with the computational effort, this work also reveals the rationales why the highest ionic conductivity is achieved when the 1S3X configuration prevails at 4d sites.
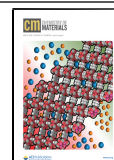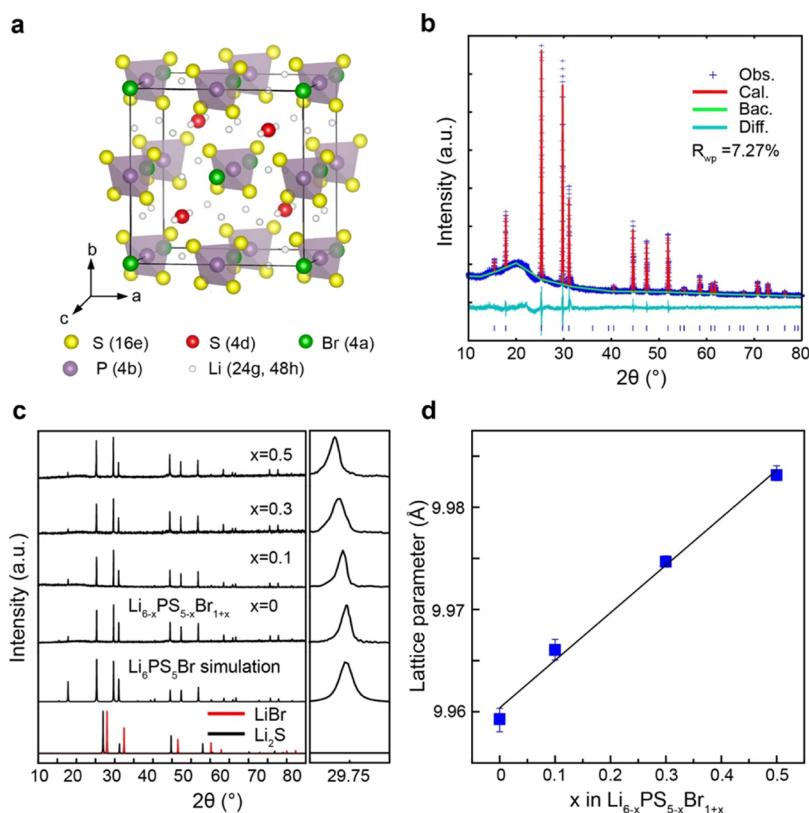
METHODS

Synthesis. Li$_2$S (99.98%, Sigma-Aldrich), P$_2$S$_5$ (99%, Sigma-Aldrich), and LiBr (99%, Sigma-Aldrich) were kept in an argon-filled glovebox (Mbraun) to avoid exposure to oxygen and moisture and were dried before use. The powder was then prepared by mixing the as-mentioned precursors using an agate mortar with a stoichiometric

Figure 1. XRD characterizations of $Li_{6-x}PS_{5-x}Br_{1+x}$ ($0 \leq x \leq 0.5$). (a) Crystal structure of Li_6PS_5Br. Two types of S^{2-} sites are shown: free S^{2-} (Wyckoff 4d) and S^{2-} within the PS_4^{3-} tetrahedra (Wyckoff 16e). Li ions at different sites are not differentiated for simplicity. (b) High-resolution XRD of Li_6PS_5Br and the corresponding Rietveld refinement. (c) XRD patterns of $Li_{6-x}PS_{5-x}Br_{1+x}$ and expanded region around the peak (311) as a function of x ($0 \leq x \leq 0.5$). (d) Lattice parameter a obtained from the refinement of XRD patterns in (c) as a function of x in $Li_{6-x}PS_{5-x}Br_{1+x}$.

ratio. The mixture was then sealed in an airtight quartz tube in argon. The sealed tube was placed in a box furnace and heated from room temperature to 300 °C at a rate of 1 °C min^{-1}. The temperature was kept at 300 °C for 12 h. Then, the heat-treated powder was ground again and pressed into a pellet using a 6 mm stainless-steel mold. The pellet was sintered at 450−550 °C for 12 h under vacuum.

Electrochemical Measurements. The pellet was sandwiched by two indium blocking electrodes and then assembled into a cylindrical cell. Electrochemical impedance spectroscopy (EIS) was performed using a Gamry Reference 600+ with frequencies from 1 Hz to 5 MHz. The conductivity was calculated with $\sigma = \frac{L}{S \times R}$, where L, S, and R are the thickness (cm), contact area (cm^2), and resistance (ohm). The temperature-dependent impedance measurements were carried out using a CSZ MicroClimate chamber within the range of 20−120 °C.

X-ray Diffraction. The pellet was ground into powder and transferred to an X-ray diffraction (XRD) holder in an argon-filled glovebox. The holder containing the sample was sealed using vacuum grease and Kapton film. The powder XRD measurements were performed on a PANalytical X'PERT Pro powder diffractometer (Cu $K\alpha_1$, $\lambda = 1.5406$ Å) at 45 kV and 40 mA at ambient temperature. The scanning speed is 1.16° min^{-1} within the range of $2\theta = 10−80°$. Rietveld refinement was carried out on the X-ray powder pattern of Li_6PS_5Br using GSAS II software.[18] The following parameters were refined stepwise: (1) scale factor, (2) zero shift error, (3) background using Chebyshev function with six free parameters, (4) peak shape described as pseudo-Voigt function, (5) lattice constants, (6) atom coordinates, and (7) isotropic thermal displacement (U_{iso}) parameters. Fractional occupancies of the anions Br$^-$ and S^{2-} (4a vs 4d sites) were refined by adding constraints in the U_{iso} parameters with the sum of occupancy set as 1.

Tracer Exchange. The Li_6PS_5Br pellet was sandwiched by two ^6Li foils to assemble into a cylindrical cell. The cell was cycled 100 times

using an Abrin battery testing system with a current density of 10 μA cm^{-1}, and the direction of current was changed every 30 min.

Solid-State NMR Measurements. The $^{6/7}Li$ and ^{31}P magic-angle spinning (MAS) NMR measurements were carried out on a Bruker AVANCE III-500 spectrometer with the powdered samples packed in 2.5 mm zirconia rotors spun at 25 kHz. The $^{6/7}Li$ spectra were collected using a single-pulse sequence, and a spin-echo sequence was used to obtain ^{31}P spectra. The chemical shifts of $^{6/7}Li$ and ^{31}P spectra were referenced to solid LiCl at −1.1 ppm and 85% H_3PO_4 solution at 0 ppm, respectively. The static ^{79}Br quadrupolar Carr−Purcell−Meiboom−Gill (QCPMG) NMR spectra were acquired on an 830 MHz (19.6 T) spectrometer using a home-built 3.2 mm probe. The ^{79}Br shifts were referenced to solid KBr at 54.5 ppm.

Density Functional Theory Calculations. All density functional theory (DFT) energy calculations, NMR shielding tensor calculations, and ab initio molecular dynamics (AIMD) were performed in the Vienna ab initio simulation package (VASP) using the projector augmented wave (PAW) approach.[19,20] Perdew−Burke−Ernzerhof generalized-gradient approximation (GGA-PBE) was used as the exchange−correlation functional, with the latest PAW potential files available in the VASP.[21] For $Li_{6-x}PS_{5-x}Br_{1+x}$, an electrostatic energy criterion was used to prescreen structures with different Li$^+$/vacancy, S^{2-}/Br$^-$ orderings based on the pristine structure of Li_6PS_5Br taken from the Materials Project (ID: mp-985591).[22] Based on the stoichiometry, 20 lowest electrostatic energy structures were generated at each concentration interval ($x = 0$, 0.125, 0.25, 0.375, 0.5, 0.625, 0.75) in a $2 \times 1 \times 1$ supercell using the Python Materials Genomics (pymatgen) package[23] and further optimized in DFT calculations. Details of the atomic arrangement can be found in Table S2 in the Supporting Information. Geometry optimization and total energy calculations were conducted with a plane-wave cutoff of 520 eV and a k-point sampling of $1 \times 2 \times 2$ for unit cells consisting of 98−106 atoms. The unit cell parameters were relaxed during structural
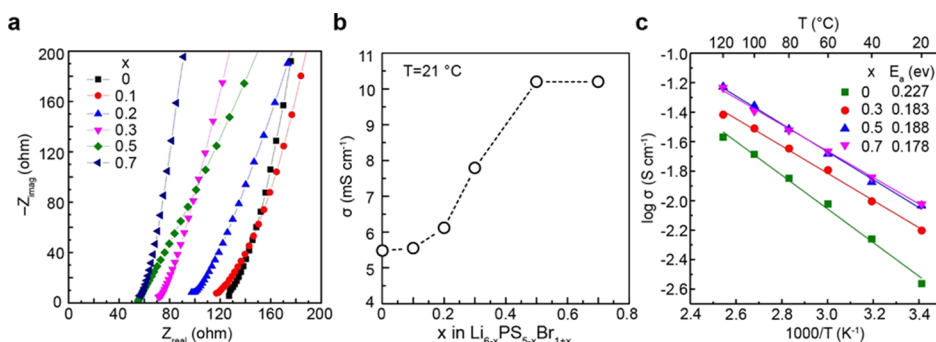
Figure 2. Electrochemical impedance and ionic conductivity of $Li_{6-x}PS_{5-x}Br_{1+x}$ ($0 \leq x \leq 0.7$). (a) Electrochemical impedance measured at 21 °C. (b) Ionic conductivity of $Li_{6-x}PS_{5-x}Br_{1+x}$ as a function of x ($0 \leq x \leq 0.7$). (c) Arrhenius plot of the ionic conductivity of $Li_{6-x}PS_{5-x}Br_{1+x}$ ($x = 0, 0.3, 0.5$, and 0.7) as a function of temperature.
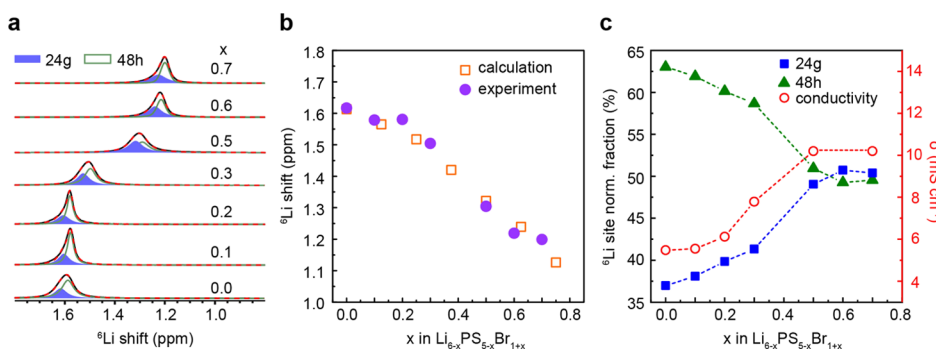
Figure 3. ^6Li NMR characterization of $Li_{6-x}PS_{5-x}Br_{1+x}$. (a) Li at 24g and 48h Wyckoff sites observed with ^6Li NMR. (b) ^6Li isotropic NMR shifts obtained from experiments compared with ^6Li shifts obtained with DFT NMR calculations. (c) Normalized ^6Li NMR resonance integrals of Li (24g) and Li (48h) in $Li_{6-x}PS_{5-x}Br_{1+x}$ and the corresponding ionic conductivities.

optimization. Chemical shifts were calculated using the linear response method developed by Yates, Pickard, and Mauri.[24,25] Structures with the lowest total energy were used for chemical shift calculation. The AIMD simulations[26] were performed on the canonical ensemble with a time step of 2 fs, and the temperature was initialized at 100 K and elevated to the appropriate temperature with simulations over 100 ps for statistical analysis.

RESULTS AND DISCUSSION

The long-range structures of $Li_{6-x}PS_{5-x}Br_{1+x}$ are studied with XRD. Figure 1a shows an ideally ordered argyrodite structure with no mixing of S^{2-} and Br^-. S^{2-} occupies two different Wyckoff sites, which are 16e sites located within PS_4 units and 4d sites in the second coordination sphere of P (4b). Because of the similar ionic radii (S^{2-}: 0.184 nm; Br^-: 0.196 nm), S^{2-} (4d) can exchange with Br^- at the 4a positions, which leads to anion disorder at 4a and 4d sites. On the other hand, the PS_4 units are rigid with strong covalent bonds between P and S; thus, substitution of S^{2-} (16e) with halide ions is rare. In each unit cell, there are 24 Li^+ which can show a positional disorder over 24g and 48h sites. 48h sites are off-center positions within the S_3Br tetrahedra. In the middle of the common plane of two face-sharing S_3Br tetrahedra lie the 24g sites.[27] It should be noted that the distance between two 48h Li ions is 0.19 nm, so it is not energetically favorable for Li ions to simultaneously occupy both 48h sites within the face-sharing double tetrahedra of S_3Br.[28] Therefore, Li ions only reside at either the 48h sites or the 24g sites within the double tetrahedra. Twenty four Li ions spread out around the 4d positions, and every 6 Li ions construct a cage-like octahedron. Li-ion transport can occur within a 48h pair (doublet) between

different 48h pairs within the cage (intracage) and/or between different cages (intercage).[15] Crystalline $Li_{6-x}PS_{5-x}Br_{1+x}$ ($0 \leq x \leq 0.5$) was obtained at the annealing temperature of 450–550 °C.. Figure 1b is the Rietveld refinement of high-resolution XRD pattern of Li_6PS_5Br. It shows that 24.4% of 4d sites are taken by Br (Table S1), indicating considerable site disorder. With the increasing amount of Br, the cubic structure is maintained with enlargement of the lattice parameter. Taking the (311) plane as an example (Figure 1c), the shift of the (311) diffraction peak around 30° to smaller angles indicates that the lattice experiences an expansion, which can potentially lead to enlarged ion diffusion channels. The lattice parameter as a function of Br amount is plotted, which is in accordance with Vegard's law (Figure 1d). It is worth mentioning that $Li_{5.3}PS_{4.3}Br_{1.7}$ and $Li_{5.2}PS_{4.2}Br_{1.8}$ are also synthesized, but both samples contain the impurity phase LiBr. The XRD patterns are shown in Figure S1. The nominal $Li_{5.3}PS_{4.3}Br_{1.7}$ shows similar structural and functional properties as $Li_{5.5}PS_{4.5}Br_{1.5}$, except a slight difference in Li^+ distribution in the structures. For the sake of completeness, $Li_{5.3}PS_{4.3}Br_{1.7}$ is included in the following discussion.

Based on the EIS measurements of $Li_{6-x}PS_{5-x}Br_{1+x}$ (Figure 2a), the ionic conductivity ($T = 21$ °C) increases from Li_6PS_5Br to $Li_{5.3}PS_{4.3}Br_{1.7}$ and then decreases in $Li_{5.2}PS_{4.2}Br_{1.8}$ because of significant structural change, as evidenced in the XRD patterns (Figure S1). The highest ionic conductivity of 10 mS cm^{-1} at 21 °C is achieved in $Li_{5.3}PS_{4.3}Br_{1.7}$, which doubles that of Li_6PS_5Br. Figure 2c exhibits the temperature dependence of the ionic conductivity of $Li_{6-x}PS_{5-x}Br_{1+x}$. Li_6PS_5Br shows the highest activation energy of 0.227 eV, and $Li_{5.3}PS_{4.3}Br_{1.7}$ has the lowest activation energy of 0.178 eV.

To probe structural disorder and moreover to understand the origin of ionic conductivity enhancement, multinuclear high-resolution solid-state NMR is applied. Two Li resonances are observed in the ^{6}Li NMR spectra of $Li_{6-x}PS_{5-x}Br_{1+x}$ (Figure 3a). The 1.62 ppm resonance is assigned to Li (24g) and the one at 1.59 ppm is assigned to Li (48h) in Li_6PS_5Br. The small difference in the chemical shift stems from slightly different deshielding effects on Li at 24g and 48h sites. To confirm this spectral assignment, two different Li_6PS_5Br structures are simulated to investigate the difference between the resonances of Li (24g) and Li (48h) in ^{6}Li NMR spectra: Li ions locate exclusively at 24g and exclusively at 48h sites, respectively. The NMR calculation results show that the resonance of Li (24g) has a larger isotropic shift than that of Li (48h) (Figure S3), which verifies our assignment of the two Li signals in ^{6}Li spectra. With the increasing amount of Br$^-$, more S^{2-} at 4d sites are substituted by Br$^-$, which introduces Li vacancies in the cages surrounding the 4d positions. The ^{6}Li signal shifts toward higher field with smaller parts per million (ppm) values. Figure 3b shows that the ^{6}Li isotropic shift is in agreement with the average ^{6}Li shift obtained from DFT NMR calculations. Figure 3c presents the fractions of Li (24g) and Li (48h) resonance integrals in $Li_{6-x}PS_{5-x}Br_{1+x}$ together with the corresponding ionic conductivities. An increase in the fraction of Li (24 g) resonance is observed with the increasing x value in $Li_{6-x}PS_{5-x}Br_{1+x}$. This suggests increased disorder in Li occupancies, induced by Br$^- \rightarrow$ S^{2-} substitution. The nature of this disorder can be both dynamic and static, supported by the experimental evidence and computational investigations presented in the following.

Li-ion dynamics in $Li_{6-x}PS_{5-x}Br_{1+x}$ ($0 \leq x \leq 0.7$) is probed with NMR spin−lattice relaxation time (T_1) measurements. According to the Bloembergen, Purcell, and Pound relaxation model,[29] the correlation time (τ_c) and T_1 are related through eq 1 where γ is the magnetogyric ratio, $\hbar$ is the reduced Planck constant, r_0 is the interatomic distance, and ω_0 is the Larmor frequency. In the fast motion region, $\omega_0\tau_c \ll 1$, eq 1 can be simplified to eq 2. An attempt jump frequency ($1/\tau_{c,0}$) on the magnitude of 10^{12} s^{-1} is observed for Li_6PS_5Br, suggesting a liquid-like dynamic behavior.[30] Therefore, $\omega_0\tau_c \ll 1$ is satisfied, and based on eq 2, large T_1 values suggest fast Li-ion motion. Figure 4 shows T_1 of $Li_{6-x}PS_{5-x}Br_{1+x}$ as a function of x. With increasing Br in $Li_{6-x}PS_{5-x}Br_{1+x}$, ^{7}Li T_1 increases, suggesting increased Li-ion motion. The enhanced Li-ion
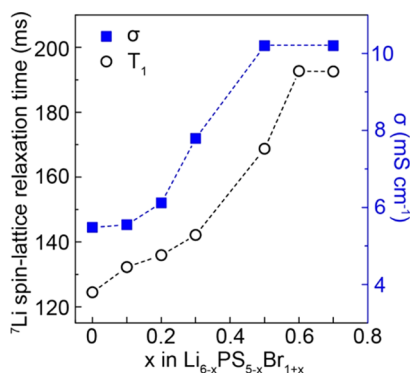
motion will facilitate Li-ion conduction; this echoes with the observation of increased Li-ion conductivity.

$$\left(\frac{1}{T_1}\right) = \frac{3\gamma^4\hbar^2}{10r_0^6}\left[\frac{\tau_c}{1+\omega_0^2\tau_c^2} + \frac{4\tau_c}{1+4\omega_0^2\tau_c^2}\right] \tag{1}$$

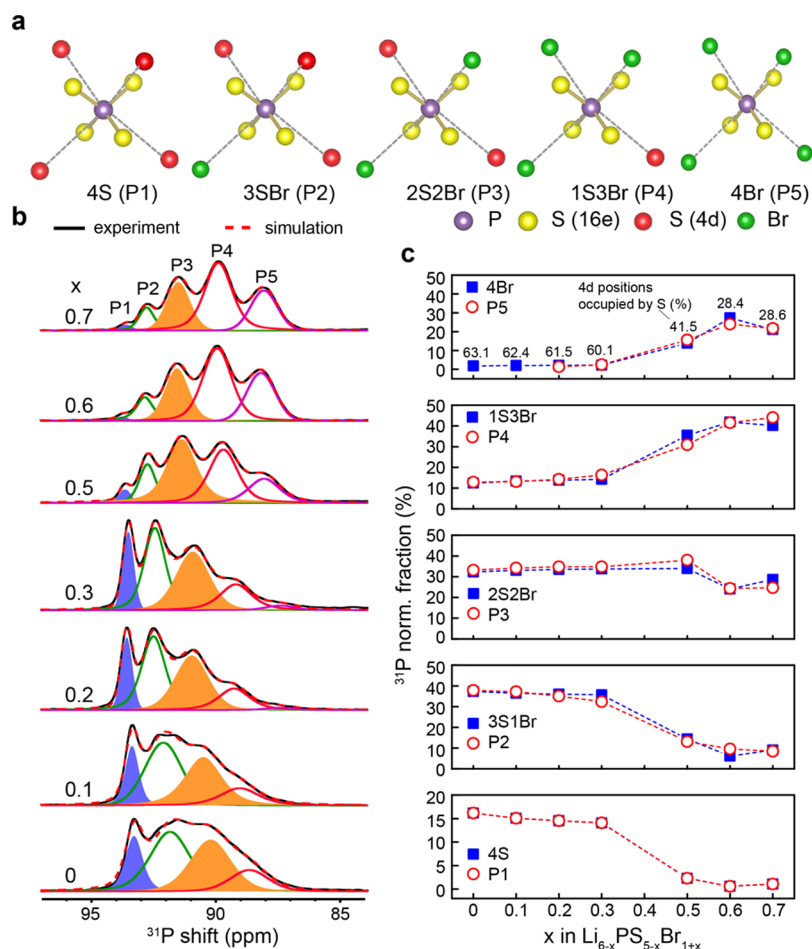$$\left(\frac{1}{T_1}\right) = \frac{3}{2}\frac{\gamma^4\hbar^2}{r_0^6}\tau_c \tag{2}$$

To examine the Br$^-$/S^{2-} disorder at 4d sites, ^{31}P NMR is employed. In the $Li_{6-x}PS_{5-x}Br_{1+x}$ structure, four 4d sites located in the second coordination shell of P can be occupied by either S^{2-} or Br$^-$. The difference can be manifested in ^{31}P NMR resonances. Figure 5a shows five distinctive arrangements at the four 4d sites: 4S, 3S1Br, 2S2Br, 1S3Br, and 4Br. Correspondingly, five ^{31}P NMR resonances are detected (Figure 5b): P1 (4S), P2 (3S1Br), P3 (2S2Br), P4 (1S3Br), and P5 (4Br). Significant disorder is observed even at low Br concentration from ^{31}P NMR spectra. Notably, the resonance of the P5 component is undetectable at low Br content; however, starting from $x = 0.3$, all five characteristic local environments of P are shown. The P1 (4S) peak is well-resolved in the ^{31}P NMR spectra across the whole set of $Li_{6-x}PS_{5-x}Br_{1+x}$ samples, and its intensity decreases with the increasing amount of Br. Assuming statistically random mixing of Br$^-$ and S^{2-} at 4d sites, the probability of each configuration is calculated using

$$P(nS(4-n)Br) = \frac{4!}{n!(4-n)!}y^n(1-y)^{4-n} \tag{3}$$

where n (n = 0, 1, 2, 3, 4) and y ($0 \leq y \leq 1$) represent the number of sulfur at the 4d sites and the fraction of 4d sites occupied by S, respectively. The experimental data of ^{31}P NMR are in agreement with the predicted fractions of five configurations (Figure 5c), which confirm that the peak of P(5 − n) reflects the configuration of $nS(4 - n)$Br. Among these five configurations, the fractions of 1S3Br and 4Br increase from $x = 0$ to 0.7. 4S and 3S1Br slightly decrease in the beginning and then drop abruptly from $x = 0.3$ to 0.5. The change in the fraction of 2S2Br configuration is less significant relative to other configurations. In summary, Br$^-$/S^{2-} occupies 4d sites in a statistically random fashion. Therefore, with increasing Br$^-$ amount in the structure, more Br$^-$ is observed to reside at 4d sites, enhancing S^{2-}/Br$^-$ disorder.

The disorder of Br$^-$ and S^{2-} at 4d sites can also be directly probed with ^{79}Br NMR. However, ^{79}Br (spin-3/2) spins often exhibit a large quadrupolar moment, which significantly broadens ^{79}Br NMR resonance over thousands of ppm with low resolution. Accurate quantification is difficult because of the challenges in achieving homogeneous broadband excitation and high resolution. The broad ^{79}Br resonance of $Li_{6-x}PS_{5-x}Br_{1+x}$ can extend up to 2000 ppm, which has a spin−spin relaxation time (T_2) of several microseconds, posing tremendous challenge in data acquisition. The signal that decays in several microseconds is hard to capture by regular single-pulse or spin-echo NMR experiments. Therefore, a QCPMG pulse sequence is utilized to enhance the signal-to-noise ratio with broad excitation at the expense of resolution, and the acquired ^{79}Br NMR spectra are shown in Figure S2. A previous ^{79}Br NMR study on Li_6PS_5Br has shown a sharp signal (109 ppm) and a broad signal (−40 ppm) that are assigned to "ordered" and "disordered" structures, respec-

Figure 4. ^{7}Li NMR spin−lattice relaxation time (T_1) as an indicator of Li-ion dynamics. The measured ionic conductivity is also plotted for comparing the trend.

Figure 5. (a) Five different configurations of Wyckoff 4d sites in the second coordination shell of P. (b) Five characteristic P local structural environments observed with ^{31}P NMR denoted as P1−P5, representing P with the closest four 4d sites occupied by 4S, 3SBr, 2S2Br, 1S3Br, and 4Br, respectively. (c) Normalized fractions of P1−P5 structural environments based on ^{31}P NMR analysis (red open circles) compared with predicted values by statistical distribution calculation (blue filled squares). Corresponding fractions of 4d sites occupied by sulfur are shown in the top box.
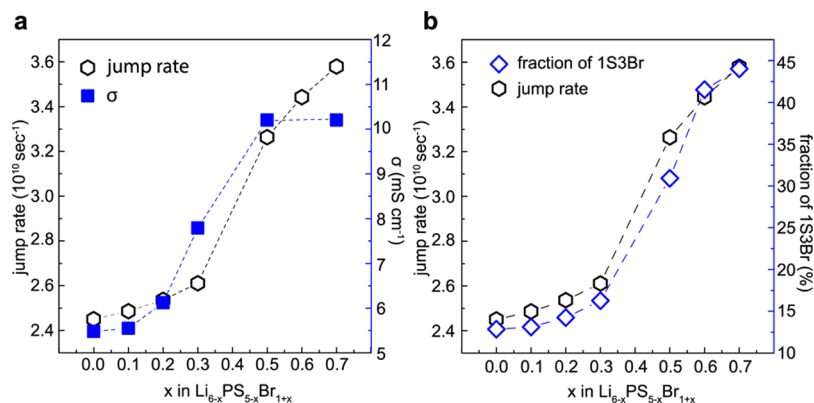

Figure 6. (a) Overall jump rate and conductivity as a function of x in $Li_{6−x}PS_{5−x}Br_{1+x}$. (b) Fraction of 1S3Br as a function of x in $Li_{6−x}PS_{5−x}Br_{1+x}$ in comparison with the overall jump rate.

tively.[6] To make reliable spectral assignments, $Li_{5.7}PS_{4.7}IBr_{0.3}$ is synthesized in this work. Because $I^−$ shows no positional mixing with $S^{2−}$ in Li_6PS_5I because of significantly larger ionic radius than $S^{2−}$ and prefers to sit at 4a sites, $Br^−$ will be forced to sit at 4d sites. The ^{79}Br NMR spectrum of $Li_{5.7}PS_{4.7}IBr_{0.3}$ shows enhanced intensity of the Br (4d) resonance. The crystallographic site 4a is a high-symmetry site; the

quadrupolar interaction is weak. As a result, the line shape of the Br (4a) resonance should be sharp. This is then used for analyzing the spectra acquired by ^{79}Br QCPMG NMR experiments. The signal from the sharp component of Br (4a) is allocated into the spikelets near 100 ppm in the QCPMG spectra, and the rest of the signals are from Br (4d). The ^{79}Br QCPMG NMR spectra of $Li_{6−x}PS_{5−x}Br_{1+x}$ reveal
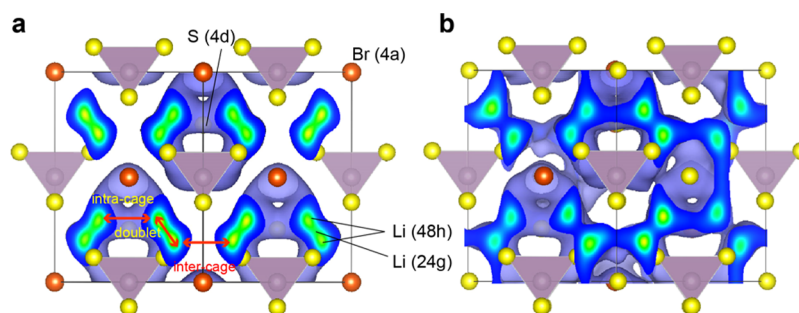
Figure 7. Li density distribution in Li_6PS_5Br with (a) 0 and (b) 50% of the 4d sites occupied by Br^- in a $1 \times 1 \times 1$ cell based on AIMD simulations at 500 K.
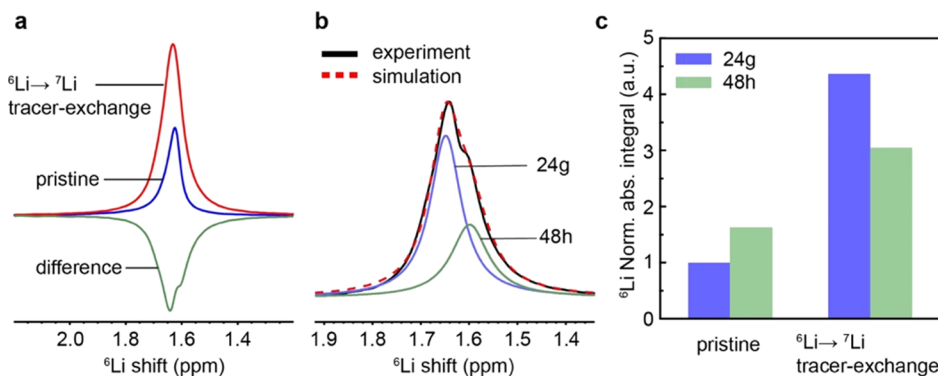
Figure 8. Tracer-exchange Li NMR. (a) ^6Li NMR of the pristine and $^6Li \rightarrow {}^7Li$ tracer-exchanged Li_6PS_5Br. (b) Simulation of the difference spectrum. (c) Normalized spectral integrals of ^6Li NMR resonances from Li at 24g and 48h sites.

gradual increase in Br occupancy at 4d sites (Figure S2a) with increasing x. Figure S2b summarizes the fraction of 4d sites occupied by Br from ^{31}P and ^{79}Br NMR analyses, which are in good agreement. It shows that the Br (4d) occupancy positively correlates with Br amount in $Li_{6-x}PS_{5-x}Br_{1+x}$.

Different Br/S arrangements at 4d sites lead to different limiting Li jumps, that is, the slowest step among a series of Li jumps to complete the long-range diffusion. A distribution of distinctive configurations (4S, 3S1Br, 2S2Br, 1S3Br, and 4Br) at 4d sites exists in $Li_{6-x}PS_{5-x}Br_{1+x}$. All configurations should affect the overall jump rate for ion conduction. The ionic conductivity σ is a function of jump rate R, as shown in the Nernst−Einstein equation

$$\sigma = \frac{ne^2z^2}{H_R kT}D = \frac{ne^2z^2a^2}{2H_R kdT}R \qquad (4)$$

where n is the diffusing particle density, e the charge of electron, z the ionic charge, a the jump distance, d the number of diffusion dimensions, k Boltzmann's constant, T the temperature in kelvin, and H_R the Haven ratio. To correlate the jump rate with the conductivity of the bulk material based on the experimental data, the empirical overall Li-ion jump rate is estimated by

$$R_{overall} = \sum P_i \times R_i \qquad (5)$$

where P_i is the probability of a configuration at 4d sites obtained from ^{31}P NMR analysis and R_i is the limiting Li-ion jump rate of a corresponding configuration at 4d sites based on AIMD simulations (Table S4).[15] A positive correlation between the measured conductivity and the calculated overall Li-ion jump rate is found (Figure 6a) for $Li_{6-x}PS_{5-x}Br_{1+x}$. A phase-pure $Li_{5.3}PS_{4.3}Br_{1.7}$ sample is expected to exhibit higher

conductivity than the measured value; a small amount of impurities in $Li_{5.3}PS_{4.3}Br_{1.7}$ slightly decreases the ionic conductivity. The fraction of 1S3Br is side by side with the calculated overall Li-ion jump rate (Figure 6b), which follows a similar trend as increasing x in $Li_{6-x}PS_{5-x}Br_{1+x}$. It suggests that the configuration of 1S3Br is the major factor to determine the overall Li jump. This is consistent with the experimental results, showing that 70% Br-occupancy at 4d sites delivers the highest measured ionic conductivity.

AIMD simulations are employed to further understand the impact of Br^-/S^{2-} disorder on Li-ion density distribution and diffusion. $1 \times 1 \times 1$ cells with Br 4d-site occupancies of 0, 25, 50, 75, and 100% are generated, which correspond to the atomic arrangements of 4S, 3S1Br, 2S2Br, 1S3Br, and 4Br, respectively. The result shows a localized Li diffusion within individual cages when the 4d sites are fully occupied by S^{2-} (Figure 7a). However, once the occupancy of Br^- at 4d sites increases, the cages are connected, forming a diffusion pathway network (Figure 7b). To form a network for ion diffusion, all three types of Li-ion jumps should be present: doublet (within a 48h−48h pair), intracage (between neighbored 48h−48h pairs), and intercage (between two different cages).[15] This is manifested in Figure 7, in which the 0 Br-occupancy model (Figure 7a) shows a low Li density between cages, indicating the lack of intercage jumps. However, the 50% Br-occupancy model (Figure 7b) exhibits prominent intercage jumps, accompanied by the decrease in doublet jumps. As a result, the overall rate for Li diffusion is limited by intercage jumps at low Br-occupancy at 4d sites and by doublet jumps at high Br-occupancy. In other words, the overall jump rate is determined by the slowest step. This is consistent with previous reports on the Cl-argyrodite.[15] At 100% Cl/Br-occupancy at 4d sites, the frequency of the doublet jump becomes extremely low,

revealed by the decreased possibility of the presence of Li along the 48h−48h passage. Therefore, the cages get disconnected and Li diffusion becomes localized again. In summary, the S^{2-}/Br^- disorder at 4d sites influences Li distribution along different paths, which affects the formation of a 3D Li transport network.

To probe the active crystallographic sites for ion conduction, $^6Li \rightarrow {}^7Li$ tracer-exchange NMR is utilized.[31−34] The Li_6PS_5Br sample is sandwiched by two ^6Li foils. Because the electrolyte pellet is naturally abundant in ^7Li (^7Li: 92.4%, ^6Li: 7.6%), driven by a biased electric potential, ^6Li ions from ^6Li−metal can occupy the vacant/interstitial sites or partially replace the native ^7Li ions, rendering the ion transport pathways enriched by ^6Li. Figure 8a shows an increase of ^6Li signal intensity for both 24g and 48h sites but with the preference for 24g sites over 48h sites. The fitting of the difference spectrum (Figure 8b) shows 65.3% of the total intensity from Li (24g) resonance and 34.7% from Li (48h) resonance. Figure 8c is the summary of the quantitative analysis on the signals before and after tracer exchange. The intensity of the Li (24g) signal in the pristine sample is normalized to 1. The amount of ^6Li at 24g sites and 48h sites is increased by 4.37 and 1.88 times, respectively, which indicates that 24g sites are more frequently visited in ion conduction.

CONCLUSIONS

In this work, Br^-/S^{2-} mixing at 4d sites is enforced by increasing the total Br content in $Li_{6-x}PS_{5-x}Br_{1+x}$. The highest ionic conductivity of 11 mS cm^{-1} at 25 °C is achieved in $Li_{5.3}PS_{4.3}Br_{1.7}$ with a low activation energy barrier of 0.18 eV. NMR, XRD, and impedance spectroscopy are combined to unveil the origin of high ionic conductivity. The positional mixing of Br^- and S^{2-} is probed independently with ^{31}P and ^{79}Br NMR. A set of characteristic local structures of 4d sites are revealed by ^{31}P NMR, and the fraction of the structural configuration of 1S3Br at 4d sites is proven to greatly impact the overall Li^+ jump rate, which rationalizes the observation of $Li_{5.3}PS_{4.3}Br_{1.7}$ with 30% S and 70% Br at 4d sites delivering the highest measured ionic conductivity. The fraction of Li (24g) shows a positive correlation with conductivity, and $^6Li \rightarrow {}^7Li$ tracer-exchange NMR experiments confirm that Li (24g) is instrumental to ion conduction.

It is worth mentioning that enhancement in ion migration via increasing compositional and structural entropy of structural cations and/or anions has been observed in many systems beyond Li-ion conductors,[35−37] and systematic studies on the fundamental principles underlying the composition−structure−ion dynamics correlations will be invaluable for controlled engineering of functional properties.

ASSOCIATED CONTENT

Ⓢ Supporting Information

The Supporting Information is available free of charge at https://pubs.acs.org/doi/10.1021/acs.chemmater.9b05331.

> Selected Rietveld refinement data; atomic arrangements for DFT calculations; XRD patterns of $Li_{5.3}PS_{4.3}Br_{1.7}$ and $Li_{5.2}PS_{4.2}Br_{1.8}$; ^{79}Br static QCPMG NMR data; ^6Li NMR shift calculations; and jump rate calculations (PDF)

AUTHOR INFORMATION

Corresponding Author

Yan-Yan Hu − *Department of Chemistry and Biochemistry, Florida State University, Tallahassee, Florida 32306, United States; Center of Interdisciplinary Magnetic Resonance, National High Magnetic Field Laboratory, Tallahassee, Florida 32310, United States;* ⓞ orcid.org/0000-0003-0677-5897; Email: yhu@fsu.edu

Authors

Pengbo Wang − *Department of Chemistry and Biochemistry, Florida State University, Tallahassee, Florida 32306, United States*

Haoyu Liu − *Department of Chemistry and Biochemistry, Florida State University, Tallahassee, Florida 32306, United States*

Sawankumar Patel − *Department of Chemistry and Biochemistry, Florida State University, Tallahassee, Florida 32306, United States*

Xuyong Feng − *Department of Chemistry and Biochemistry, Florida State University, Tallahassee, Florida 32306, United States*

Po-Hsiu Chien − *Department of Chemistry and Biochemistry, Florida State University, Tallahassee, Florida 32306, United States; Center of Interdisciplinary Magnetic Resonance, National High Magnetic Field Laboratory, Tallahassee, Florida 32310, United States*

Yan Wang − *Advanced Material Lab, Samsung Research America, Burlington, Massachusetts 01803, United States; Department of Material Science and Engineering, Massachusetts Institute of Technology, Cambridge, Massachusetts 02139, United States*

Complete contact information is available at:
https://pubs.acs.org/10.1021/acs.chemmater.9b05331

Notes

The authors declare no competing financial interest.

ABBREVIATIONS

NMR, nuclear magnetic resonance; MAS, magic-angle spinning; EIS, electrochemical impedance spectroscopy; XRD, X-ray diffraction; DFT, density functional theory; QCPMG, quadrupolar Carr−Purcell−Meiboom−Gill; VASP, Vienna ab initio simulation package; PAW, projector augmented wave; AIMD, ab initio molecular dynamics; GGA-PBE, Perdew−Burke−Ernzerhof generalized-gradient approximation; ppm, parts per million

REFERENCES

(1) Li, J.; Ma, C.; Chi, M.; Liang, C.; Dudney, N. J. Solid Electrolyte: The Key for High-Voltage Lithium Batteries. *Adv. Energy Mater.* **2015**, *5*, 1401408.

(2) Liu, Y.; He, P.; Zhou, H. Rechargeable Solid-State Li-Air and Li-S Batteries: Materials, Construction, and Challenges. *Adv. Energy Mater.* **2018**, *8*, 1701602.

(3) Liang, J.-Y.; Zeng, X.-X.; Zhang, X.-D.; Zuo, T.-T.; Yan, M.; Yin, Y.-X.; Shi, J.-L.; Wu, X.-W.; Guo, Y.-G.; Wan, L.-J. Engineering Janus Interfaces of Ceramic Electrolyte via Distinct Functional Polymers for Stable High-Voltage Li-Metal Batteries. *J. Am. Chem. Soc.* **2019**, *141*, 9165−9169.

(4) Rao, R. P.; Adams, S. Studies of Lithium Argyrodite Solid Electrolytes for All-Solid-State Batteries. *Phys. Status Solidi A* **2011**, *208*, 1804−1807.

(5) Boulineau, S.; Courty, M.; Tarascon, J.-M.; Viallet, V. Mechanochemical Synthesis of Li-Argyrodite Li_6PS_5X (X=Cl, Br, I) as Sulfur-Based Solid Electrolytes for All Solid State Batteries Application. *Solid State Ionics* **2012**, *221*, 1−5.

(6) Deiseroth, H.-J.; Kong, S.-T.; Eckert, H.; Vannahme, J.; Reiner, C.; Zaiß, T.; Schlosser, M. Li_6PS_5X: A Class of Crystalline Li-Rich Solids With an Unusually High Li+ Mobility. *Angew. Chem., Int. Ed.* **2008**, *47*, 755−758.

(7) Yu, C.; Ganapathy, S.; van Eck, E. R. H.; van Eijck, L.; Basak, S.; Liu, Y.; Zhang, L.; Zandbergen, H. W.; Wagemaker, M. Revealing the Relation between the Structure, Li-Ion Conductivity and Solid-State Battery Performance of the Argyrodite Li_6PS_5Br Solid Electrolyte. *J. Mater. Chem. A* **2017**, *5*, 21178−21188.

(8) Kraft, M. A.; Culver, S. P.; Calderon, M.; Böcher, F.; Krauskopf, T.; Senyshyn, A.; Dietrich, C.; Zevalkink, A.; Janek, J.; Zeier, W. G. Influence of Lattice Polarizability on the Ionic Conductivity in the Lithium Superionic Argyrodites Li_6PS_5X (X = Cl, Br, I). *J. Am. Chem. Soc.* **2017**, *139*, 10909−10918.

(9) Zhou, L.; Park, K.-H.; Sun, X.; Lalère, F.; Adermann, T.; Hartmann, P.; Nazar, L. F. Solvent-Engineered Design of Argyrodite Li_6PS_5X (X = Cl, Br, I) Solid Electrolytes with High Ionic Conductivity. *ACS Energy Lett.* **2019**, *4*, 265−270.

(10) Kraft, M. A.; Ohno, S.; Zinkevich, T.; Koerver, R.; Culver, S. P.; Fuchs, T.; Senyshyn, A.; Indris, S.; Morgan, B. J.; Zeier, W. G. Inducing High Ionic Conductivity in the Lithium Superionic Argyrodites $Li_{6+x}P_{1-x}Ge_xS_5I$ for All-Solid-State Batteries. *J. Am. Chem. Soc.* **2018**, *140*, 16330−16339.

(11) Minafra, N.; Culver, S. P.; Krauskopf, T.; Senyshyn, A.; Zeier, W. G. Effect of Si Substitution on the Structural and Transport Properties of Superionic Li-Argyrodites. *J. Mater. Chem. A* **2018**, *6*, 645−651.

(12) Adeli, P.; Bazak, J. D.; Park, K. H.; Kochetkov, I.; Huq, A.; Goward, G. R.; Nazar, L. F. Boosting Solid-State Diffusivity and Conductivity in Lithium Superionic Argyrodites by Halide Substitution. *Angew. Chem., Int. Ed.* **2019**, *58*, 8681−8686.

(13) Gautam, A.; Sadowski, M.; Prinz, N.; Eickhoff, H.; Minafra, N.; Ghidiu, M.; Culver, S. P.; Albe, K.; Fässler, T. F.; Zobel, M.; Zeier, W. G. Rapid Crystallization and Kinetic Freezing of Site-Disorder in the Lithium Superionic Argyrodite Li_6PS_5Br. *Chem. Mater.* **2019**, *31*, 10178.

(14) Bernges, T.; Culver, S. P.; Minafra, N.; Koerver, R.; Zeier, W. G. Competing Structural Influences in the Li Superionic Conducting Argyrodites $Li_6PS_{5-x}Se_xBr$ ($0 \leq x \leq 1$) upon Se Substitution. *Inorg. Chem.* **2018**, *57*, 13920−13928.

(15) de Klerk, N. J. J.; Rosłoń, I.; Wagemaker, M. Diffusion Mechanism of Li Argyrodite Solid Electrolytes for Li-Ion Batteries and Prediction of Optimized Halogen Doping: The Effect of Li Vacancies, Halogens, and Halogen Disorder. *Chem. Mater.* **2016**, *28*, 7955−7963.

(16) Rayavarapu, P. R.; Sharma, N.; Peterson, V. K.; Adams, S. Variation in Structure and Li+-Ion Migration in Argyrodite-Type $Li6PS5X$ (X = Cl, Br, I) Solid Electrolytes. *J. Solid State Electrochem.* **2012**, *16*, 1807−1813.

(17) Feng, X.; Chien, P.-H.; Zhu, Z.; Chu, I.-H.; Wang, P.; Immediato-Scuotto, M.; Arabzadeh, H.; Ong, S. P.; Hu, Y.-Y. Studies of Functional Defects for Fast Na-Ion Conduction in $Na_{3-y}PS_{4-x}Cl_x$ with a Combined Experimental and Computational Approach. *Adv. Funct. Mater.* **2019**, *29*, 1807951.

(18) Toby, B. H.; Von Dreele, R. B. GSAS-II : The Genesis of a Modern Open-Source All Purpose Crystallography Software Package. *J. Appl. Crystallogr.* **2013**, *46*, 544−549.

(19) Blöchl, P. E. Projector Augmented-Wave Method. *Phys. Rev. B: Condens. Matter Mater. Phys.* **1994**, *50*, 17953−17979.

(20) Kresse, G.; Furthmüller, J. Efficient Iterative Schemes for Ab Initio Total-Energy Calculations Using a Plane-Wave Basis Set. *Phys. Rev. B: Condens. Matter Mater. Phys.* **1996**, *54*, 11169−11186.

(21) Perdew, J. P.; Burke, K.; Ernzerhof, M. Generalized Gradient Approximation Made Simple. *Phys. Rev. Lett.* **1996**, *77*, 3865−3868.

(22) Jain, A.; Ong, S. P.; Hautier, G.; Chen, W.; Richards, W. D.; Dacek, S.; Cholia, S.; Gunter, D.; Skinner, D.; Ceder, G.; Persson, K. A. Commentary: The Materials Project: A Materials Genome Approach to Accelerating Materials Innovation. *APL Mater.* **2013**, *1*, 011002.

(23) Ong, S. P.; Richards, W. D.; Jain, A.; Hautier, G.; Kocher, M.; Cholia, S.; Gunter, D.; Chevrier, V. L.; Persson, K. A.; Ceder, G. Python Materials Genomics (Pymatgen): A Robust, Open-Source Python Library for Materials Analysis. *Comput. Mater. Sci.* **2013**, *68*, 314−319.

(24) Yates, J. R.; Pickard, C. J.; Mauri, F. Calculation of NMR Chemical Shifts for Extended Systems Using Ultrasoft Pseudopotentials. *Phys. Rev. B: Condens. Matter Mater. Phys.* **2007**, *76*, 024401.

(25) Pickard, C. J.; Mauri, F. All-Electron Magnetic Response with Pseudopotentials: NMR Chemical Shifts. *Phys. Rev. B: Condens. Matter Mater. Phys.* **2001**, *63*, 245101.

(26) Wang, Y.; Richards, W. D.; Ong, S. P.; Miara, L. J.; Kim, J. C.; Mo, Y.; Ceder, G. Design Principles for Solid-State Lithium Superionic Conductors. *Nat. Mater.* **2015**, *14*, 1026−1031.

(27) Kong, S.-T.; Deiseroth, H.-J.; Maier, J.; Nickel, V.; Weichert, K.; Reiner, C. Li6PO5Br and Li6PO5Cl: The first Lithium-Oxide-Argyrodites. *Z. Anorg. Allg. Chem.* **2010**, *636*, 1920−1924.

(28) Kong, S.-T.; Deiseroth, H.-J.; Reiner, C.; Gün, Ö.; Neumann, E.; Ritter, C.; Zahn, D. Lithium Argyrodites with Phosphorus and Arsenic: Order and Disorder of Lithium Atoms, Crystal Chemistry, and Phase Transitions. *Chem.—Eur. J.* **2010**, *16*, 2198−2206.

(29) Bloembergen, N.; Purcell, E. M.; Pound, R. V. Relaxation Effects in Nuclear Magnetic Resonance Absorption. *Phys. Rev.* **1948**, *73*, 679−712.

(30) Hanghofer, I.; Gadermaier, B.; Wilkening, H. M. R. Fast Rotational Dynamics in Argyrodite-Type Li_6PS_5X (X: Cl, Br, I) as Seen by [31] P Nuclear Magnetic Relaxation—On Cation−Anion Coupled Transport in Thiophosphates. *Chem. Mater.* **2019**, *31*, 4591−4597.

(31) Zheng, J.; Tang, M.; Hu, Y.-Y. Lithium Ion Pathway within $Li_7La_3Zr_2O_{12}$-Polyethylene Oxide Composite Electrolytes. *Angew. Chem.* **2016**, *128*, 12726−12730.

(32) Zheng, J.; Dang, H.; Feng, X.; Chien, P.-H.; Hu, Y.-Y. Li-Ion Transport in a Representative Ceramic−Polymer−Plasticizer Composite Electrolyte: $Li_7La_3Zr_2O_{12}$ −Polyethylene Oxide−Tetraethylene Glycol Dimethyl Ether. *J. Mater. Chem. A* **2017**, *5*, 18457−18463.

(33) Zheng, J.; Hu, Y.-Y. New Insights into the Compositional Dependence of Li-Ion Transport in Polymer-Ceramic Composite Electrolytes. *ACS Appl. Mater. Interfaces* **2018**, *10*, 4113−4120.

(34) Zheng, J.; Wang, P.; Liu, H.; Hu, Y.-Y. Interface-Enabled Ion Conduction in $Li_{10}GeP_2S_{12}$−Poly(Ethylene Oxide) Hybrid Electrolytes. *ACS Appl. Energy Mater.* **2019**, *2*, 1452−1459.

(35) Düvel, A.; Ruprecht, B.; Heitjans, P.; Wilkening, M. Mixed Alkaline-Earth Effect in the Metastable Anion Conductor $Ba_{1-x}Ca_xF_2$ ($0 \leq x \leq 1$): Correlating Long-Range Ion Transport with Local Structures Revealed by Ultrafast 19 F MAS NMR. *J. Phys. Chem. C* **2011**, *115*, 23784−23789.

(36) Li, C.; Tscheuschner, S.; Paulus, F.; Hopkinson, P. E.; Kießling, J.; Köhler, A.; Vaynzof, Y.; Huettner, S. Iodine Migration and Its Effect on Hysteresis in Perovskite Solar Cells. *Adv. Mater.* **2016**, *28*, 2446−2454.

(37) Eames, C.; Frost, J. M.; Barnes, P. R. F.; O'Regan, B. C.; Walsh, A.; Islam, M. S. Ionic Transport in Hybrid Lead Iodide Perovskite Solar Cells. *Nat. Commun.* **2015**, *6*, 7497.